



City Research Online

City, University of London Institutional Repository

Citation: Zhang, H., Yang, X., Lu, L., Chen, J., Rahman, B. M. & Zhou, L. (2021). Comparison of the phase change process in a GST-loaded silicon waveguide and MMI. *Optics Express*, 29(3), pp. 3503-3514. doi: 10.1364/oe.413660

This is the accepted version of the paper.

This version of the publication may differ from the final published version.

Permanent repository link: <https://openaccess.city.ac.uk/id/eprint/26397/>

Link to published version: <https://doi.org/10.1364/oe.413660>

Copyright: City Research Online aims to make research outputs of City, University of London available to a wider audience. Copyright and Moral Rights remain with the author(s) and/or copyright holders. URLs from City Research Online may be freely distributed and linked to.

Reuse: Copies of full items can be used for personal research or study, educational, or not-for-profit purposes without prior permission or charge. Provided that the authors, title and full bibliographic details are credited, a hyperlink and/or URL is given for the original metadata page and the content is not changed in any way.

City Research Online:

<http://openaccess.city.ac.uk/>

publications@city.ac.uk

Comparison of the phase change process in GST-loaded silicon waveguide and MMI

HANYU ZHANG,^{1,2} XING YANG,² LIANGJUN LU,^{2,*} JIANPING CHEN,² B. M. A. RAHMAN,³ AND LINJIE ZHOU²

¹ College of Telecommunications and Information Engineering, Nanjing University of Posts and Telecommunications, Nanjing 210023, China

² State Key Laboratory of Advanced Optical Communication Systems and Networks, Shanghai Institute for Advanced Communication and Data Science, Department of Electronic Engineering, Shanghai Jiao Tong University, Shanghai 200240, China

³ Department of Electrical and Electronic Engineering, City, University of London, London EC 1V0HB, U. K.

*luliangjun@sjtu.edu.cn

Abstract: In the past decades, silicon photonic integrated circuits (PICs) have been considered a promising approach to solve the bandwidth bottleneck in optical communications and interconnections. Despite the rapid advances, large-scale PICs still face a series of technical challenges, such as large footprint, high power consumption, and lack of optical memory, resulting from the active tuning methods used to control the optical waves. These challenges can be partially addressed by combining chalcogenide phase change materials (PCMs) such as Ge₂Sb₂Te₅ (GST) with silicon photonics, especially applicable in reconfigurable optical circuit applications due to the nonvolatile nature of the GST. We systematically investigate the phase change process induced by optical and electrical pulses in GST-loaded silicon waveguide and Multimode interferometer. Using optical pulse excitation to amorphize GST has a clear advantage in terms of operation speed and energy efficiency, while electrical pulse excitation is more suitable for large-scale integration because it does not require complex optical routing. This study helps better understand the phase change process and push forward the further development of the Si-GST hybrid photonic integration platform, bringing in new potential applications.

© 2020 Optical Society of America under the terms of the [OSA Open Access Publishing Agreement](#)

1. Introduction

Silicon photonics is widely considered as one of the most promising candidates for low-cost photonic integration by leveraging the complementary metal-oxide-semiconductor (CMOS) infrastructure [1]. In recent years, a wide range of silicon photonic devices have been demonstrated on the silicon-on-insulator (SOI) platform [2-4]. However, the active tuning methods are usually based on two mechanisms: the thermo-optic effect [5, 6] and the free-carrier dispersion effect [7-9]. It is still challenging to make tunable optical devices with a small footprint and low power consumption. The introduction of new materials onto silicon for emerging applications has attracted considerable attention [10-16]. Among the various existing new materials, chalcogenide-based phase change materials (PCMs) hybrid-integrated with silicon (Si) or silicon nitride (Si₃N₄) waveguides offers a promising solution for specific applications, such as neuromorphic computing [17-20], optical switching [21-24], all-optical memory [25, 26], and reconfigurable photonic circuits resembling field-programmable gate array (FPGA) in electronics [27-29]. Ge₂Sb₂Te₅ (GST) is the most commonly used PCM and has been commercially used in both optical and electronic data storage [30, 31]. It possesses at least two phase states, namely, amorphous (aGST) and crystalline (cGST) states. The introduction of GST to silicon photonics can bring various advantages. First, GST is a nonvolatile material, which means the phase state can be maintained without any static power

consumption. Therefore, the optical routing state can be stored after tuning. Second, the refractive index contrast between the amorphous and crystalline states is very large, especially in the near-infrared telecom wavelength range. Therefore, actively tunable devices can be made very compact. Third, reversible switching between two phase states can be realized for multiple cycles at a relatively high speed. It guarantees the long-term stable operation of the devices without failure. Finally, GST can be easily deposited using radio frequency (RF) sputtering from a stoichiometric GST alloy target. It hence allows for low-cost fabrication of Si-GST hybrid photonic devices.

The phase change process is dependent on the duration time of the excitation pulse. The underlying mechanism is related to both thermal [32] and athermal effects [33]. The thermal phase transition mechanism of GST is due to the localized heating in the presence of an optical or electrical pulse. A low-power long-duration pulse heats the material above the glass transition temperature, inducing the phase change from the amorphous to the crystalline state. On the other hand, to reversely transform cGST, a shorter but higher-power pulse is necessary to generate enough heat to melt the cGST. After melting, the material is then cooled down by a fast thermal quenching process so that it eventually becomes aGST. The athermal effects can only be observed when the excitation pulse is below the picosecond range. During the crystalline to the amorphous transition, the partial covalent bonds of Ge atoms are broken by the excitation pulse to induce an atomic structure migration from an octahedral to a tetrahedral configuration. The change could be realized just by electronic excitation without the need for melting [34]. Therefore, the amorphization process can occur in only several picoseconds.

In the last five years, a lot of work has also been carried out on developing phase-change photonics using Si-GST hybrid integration, where optical or electrical pulses are often used to induce the phase change. The basic waveguide structures are strip waveguide [35-38] and multimode interferometer (MMI) [39-41]. However, the difference in the phase transition process through optical and electrical excitation has not been fully investigated. In this article, we compare the basic optical properties and dynamic responses under optical and electrical pulses. Our experimental results and analyses serve to provide a reference for new device design based on the hybrid integration of silicon and GST.

2. Results and discussions

2.1 Basic optical properties

The influence of GST cell dimensions, namely, length and width, on the amorphization and crystallization processes in GST-loaded silicon nitride waveguides has been computationally studied [42]. The GST thickness is usually fixed at 10-20 nm. A thicker GST in principle gives a higher extinction coefficient and larger effective refractive index difference between amorphous and crystalline states. In this section, we investigated the influence of GST layer thickness on the insertion loss (IL) and the switching extinction ratio (ER) for silicon strip waveguide and MMI. It should be noted that we choose silicon instead of silicon nitride waveguides because it better controls the phase state of GST when using electrical pulses, which will be discussed in Section 2.3.

Figure 1(a) shows the structures of a silicon strip waveguide and an MMI loaded with a small patch of GST. The silicon device layer thickness is 0.22 μm . The strip waveguide width is 0.5 μm . The MMI is 2 μm wide and 12.4 μm long. It is connected to 0.5- μm -wide input and output strip waveguides through linear tapers with a broadened end width of 1.7 μm . The GST on the strip waveguide is a 0.5 \times 1 μm^2 rectangle and the GST on the MMI is a disk with a 1 μm diameter. An indium-tin-oxide (ITO) layer with the same thickness as GST is put on top of the GST to prevent its oxidation in the air. As the MMI is based on the self-imaging principle, the input light spot is periodically reproduced in the MMI region. Therefore, positioning the GST cell at the point of focus can yield a substantial overlap with the optical wave and thus high tuning efficiency.

We first studied the basic optical properties of both devices through numerical simulations. The operational wavelength was chosen to be $1.55 \mu\text{m}$. The refractive indices of the materials used in the simulations were adopted from [14]. Figure 1(b) shows the magnitude of the electrical field intensity ($|E|^2$) distributions in the x - z plane for the silicon strip waveguide when the GST is amorphous (left) and crystalline (right). The GST is 30 nm thick. The fundamental transverse electric (TE) mode of the silicon waveguide is launched into the input waveguide. As a comparison, Fig. 1(c) shows the results for the MMI with the same thickness of GST. In both devices, optical transmission is highly attenuated when GST becomes crystalline.

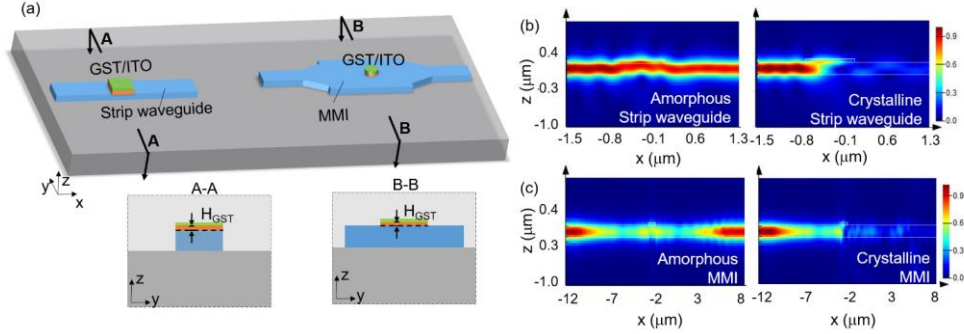


Fig. 1. (a) Schematic structures of a strip waveguide (left) and an MMI (right) with a small GST cell on top. Insets show the cross-section of the GST-loaded section. (b, c) Simulated electrical field intensity distributions in (b) the strip waveguide and (c) the MMI when the GST is amorphous (left) and crystalline (right).

Figure 2(a) shows the simulated transmission spectra of the strip waveguide and the MMI. The strip waveguide has a lower loss in the amorphous state. The MMI has a higher transmission contrast between the crystalline and amorphous states. We also performed 3D finite-difference time-domain (FDTD) simulations to obtain reflection, transmission, and absorption power with different thicknesses of GST for amorphous and crystalline states, as shown in Figs. 2(b) and 2(c), respectively. The absorption loss was calculated by subtracting the transmission and reflection power from the input one. With a thicker GST, the absorption losses in both waveguides increases, and the optical transmission contrast between the two states also increases. However, a thicker GST layer also gives a higher optical attenuation in the amorphous state. Figure 2(d) shows the on/off extinction ratio of the two waveguides. We extracted the light electric field intensity distributions at the interface between cGST and silicon, depicted in Fig. 2(e). The interfaces are marked with black dash-lines in the insets of Fig. 1(a). Since GST has a higher refractive index than silicon, the electric field is easily trapped in this layer and is subsequently absorbed due to the higher absorption coefficient. For a thicker GST, more electric field is localized in the front part of the GST cell in the strip waveguide, suggesting that a smaller portion of GST is interacting with the electric field. This phenomenon is not as pronounced in the MMI. Figure 2(f) shows the light electric field profiles along the white dashed lines denoted in Fig. 2(e) (light propagation direction).

2.2 Dynamic responses to optical pulses

The optical transmission simulations only give the steady-state optical field distribution and provide us no information about the dynamic thermal response during the phase change process. In the above simulations, we assumed that the GST reaches a fully crystalline or amorphous state. In this section, we study the dynamic thermal response for the two types of waveguides in the presence of an optical pump pulse. The pump pulse comes from the same waveguide and evanescently interacts with GST. We developed a comprehensive 3D finite element method (FEM) model to study the optical-thermal interactions in both waveguides for energy efficiency and operation speeds. For this simulation, an "Electromagnetic Waves Beam Envelopes" model from COMSOL was used to calculate the power absorbed in the GST and ITO, while the Heat

"Transfer in Solids" model was employed to calculate the temperature distribution. Here, thermal simulation is employed to predict the temperature distribution. Although it is not considered in this study, local nucleation and growth should be taken into consideration for more complete amorphization process simulation [43]. Table 1 summarizes the material properties. The refractive indices of GST in both states linearly change with temperature (T) [38]. The resistivity and thermal conductivity of GST have a nonlinear relationship with temperature [44].

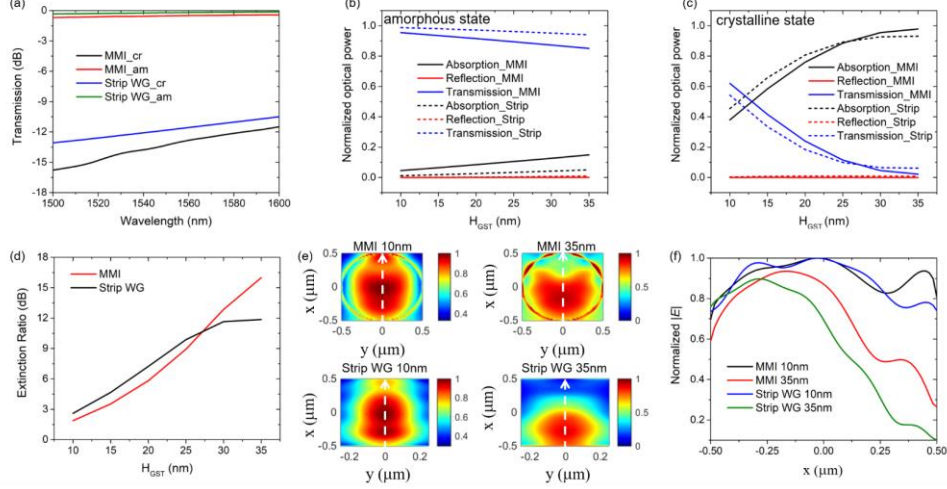


Fig. 2. (a) Simulated transmission spectra of the strip waveguide and the MMI loaded with amorphous and crystalline GST. (b, c) Normalized optical transmission, reflection, and absorption power in the Si-GST hybrid waveguide when GST is (b) amorphous and (c) crystalline. (d) On/off switching extinction ratio between amorphous and crystalline states as a function of GST thickness. (e) Normalized electric field intensity contour distributions at the interface between cGST and silicon for the MMI and the strip waveguide. The GST layer thickness is 10 nm (left) and 35 nm (right). (f) Electric field intensity profiles along the white dashed lines denoted in (e).

Table 1: Basic material properties

Material	Si	SiO ₂	ITO	aGST	cGST
Heat capacity (J/(kg·K))	720	740	340	210	210
Thermal conductivity (W/(m·K))	149	1.38	11	Variable ^a	Variable ^a
Density (kg/m ³)	2330	2200	7100	6150	6150
Complex refractive index	3.48	1.45	1.50+0.20i	$n=3.94+1.11 \times 10^{-3}T^b$ $k=0.045+4.1 \times 10^{-4}T^b$	$n=6.11-2.20 \times 10^{-4}T^b$ $k=0.83+1.56 \times 10^{-3}T^b$

^a Thermal conductivity of GST changes with temperature^[44].

^b Complex refractive index of GST changes with temperature^[38].

We first compared the optical pump pulses required for the strip waveguide and the MMI. The GST layer thickness is 30 nm. Since the amorphization temperature ($\sim 600^\circ\text{C}$) is much higher than the crystallization temperature ($\sim 160^\circ\text{C}$), GST can easily get degraded during the amorphization process. Amorphization can be induced by a single pulse, but crystallization needs several pulses to reach a fully crystalline state. In this work, we only simulate the thermal process during amorphization under a single optical pulse. Figures 3(a) and 3(c) show the GST temperature (the maximum point) change in response to an excitation optical pulse with varying amplitude. The pulse duration is fixed at 20 ns. The inset presents the 2D temperature distribution in the lateral cross-section of the GST layer at the falling edge of the optical pulse. With higher optical power, a larger amorphized GST zone can be obtained. Figures 3(b) and 3(d) show the temperature variation along the ridgelines (light propagation direction) denoted in Figs. 3(a) and 3(c), respectively. The temperature distribution is nonuniform. It suggests that

the central part of GST will be amorphized first and can easily be destroyed if attempts are made to amorphize the entire GST cell.

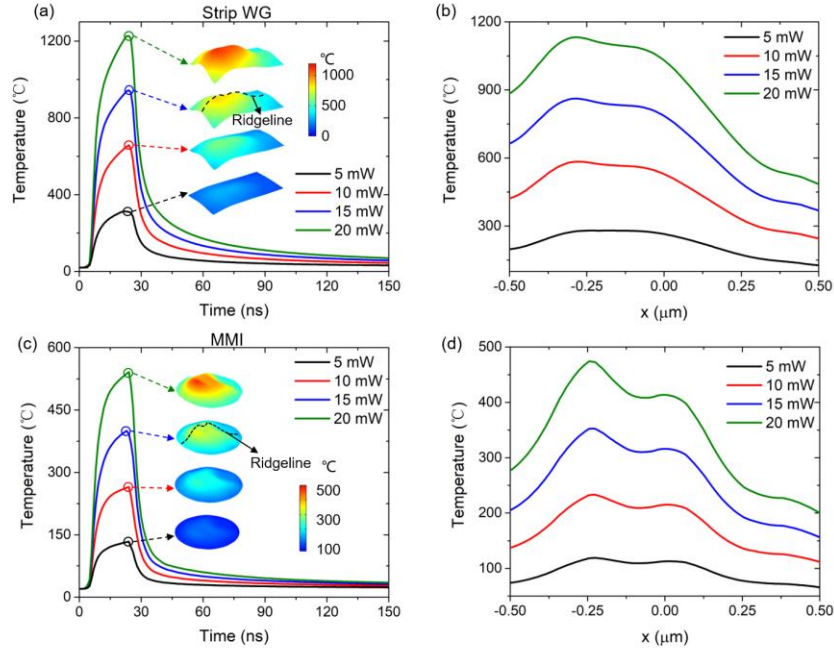


Fig. 3. (a, c) GST temperature change in response to an excitation optical pulse of different peak power for (a) strip waveguide and (c) MMI. Insets: temperature profiles in the planar cross-section of the GST layer. (b, d) Temperature distribution along the ridgelines for (b) strip waveguide and (d) MMI.

Figure 4(a) shows the maximum temperature change as a function of pump pulse power. The strip waveguide has lower power consumption. With an identical optical pump pulse, the GST temperature of the strip waveguide is around 2.3-2.6 times that of the MMI. Because silicon has higher thermal conductivity than silicon dioxide and air, the MMI section provides good thermal leakage, leading to a lower temperature. The temperature rises linearly with increased pump pulse power. By controlling the pump pulse power, we can get multiple intermediate states with a mixture of crystalline and amorphous GST. This characteristic increases the waveguide tuning freedom that can be employed to perform multiplication and logic computation [45]. We further analyze the temperature gradient ΔT (the maximum and minimum temperature difference) within the GST. Figure 4(b) shows the temperature gradient along the ridgeline and GST thickness (vertical) directions. The temperature gradient along both directions increases with the pump pulse power and is higher for the strip waveguide than for the MMI. Figure 4(c) compares the transient temperature responses for the two waveguides when they are raised to the same temperature. The type of structure has an apparent effect on the response time. The GST temperature in the MMI rises a little faster, probably because the light spot is imaged in the MMI. Meanwhile, it also cools down faster because the wide MMI section provides a faster thermal dissipation rate. The device operation speed is dominated by the dead time, which is defined as the $1/e$ cooling time.

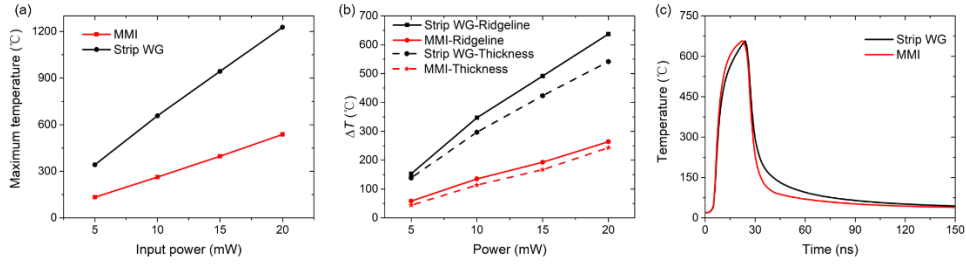


Fig. 4. (a) The maximum GST temperature as a function of optical pump pulse power. (b) Temperature gradient along the ridgeline and the GST thickness direction as a function of pump pulse power. (c) Comparison of GST temperature response to an optical pump pulse for the two waveguides.

GST layer thickness also significantly affects power consumption and operation speed. Figure 5(a) compares the GST temperature transient response for two thicknesses of GST. The amorphization pulse has a 20 ns duration and 10 mW peak power. Figure 4(b) shows the temperature profiles along the ridgelines denoted in Fig. 5(a). We see that a thicker GST layer can absorb more energy, resulting in a higher temperature. Figure 5(c) shows the maximum temperature changes as a function of the GST thickness. With the same thickness of GST, its temperature in the strip waveguide is 2.5-3.1 times higher than that in the MMI. To get the same degree of amorphization, the optical pump power required by the MMI is more than 2.5 times higher than that of the strip waveguide. This is due to the faster thermal dissipation rate in MMI. Figure 5(d) shows the temperature gradient within GST material along the ridgeline and the GST thickness direction. The temperature gradient in both directions increases with the GST thickness. More importantly, as there is a large gradient in temperature, switching the entire GST cell is more difficult when the GST layer is thick, especially in the strip waveguide. Complete amorphization is hard to obtain for a longer than 1 μm GST cell.

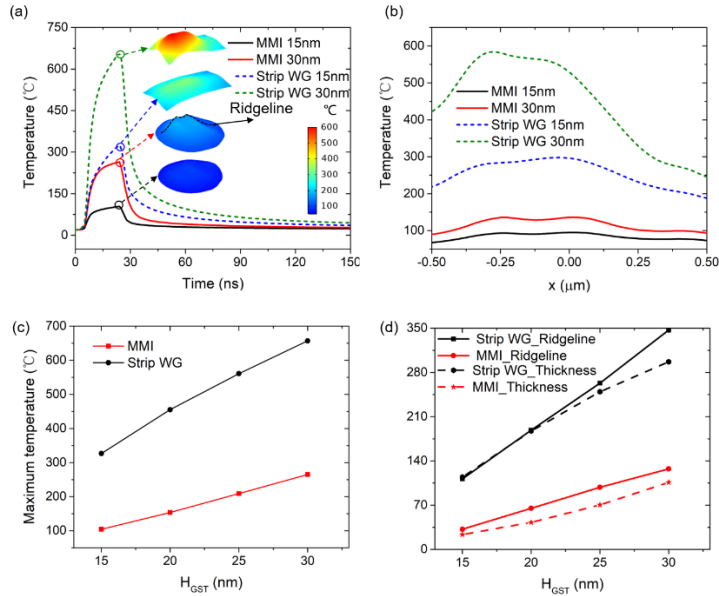


Fig. 5 (a) GST temperature transient response for two thicknesses of GST. Insets: temperature profile in the planar cross-section of the GST layer. (b) Temperature distribution along the ridgelines. (c) The maximum temperature change as a function of GST thickness. (d) Temperature gradient along the ridgeline and the GST thickness direction as a function of GST thickness.

To verify our simulation predictions, we fabricated two strip waveguides with 30-nm-thick (D1) and 15-nm-thick (D2) GST. To tolerate the misalignment between two electron beam lithography steps, we deposited a GST layer wider than the 500-nm-wide waveguide to cover the whole waveguide. Since most of the optical power is concentrated in the waveguide center, the phase change and degradation phenomenon should be similar to the waveguide only covered with GST on top. The devices were heated for 5 min at 200°C on a hot plate to reach a fully crystalline state. Figure 6(a) shows the SEM images of D1 with fully crystalline state GST. We first investigated the amorphization process of D2 when a rectangular optical pulse was applied. The optical pulse has a fixed duration of 20 ns. Figures 6(c) and 6(d) present the SEM images of the D2 when the peak power of the optical pulse power is 75 mW and 150 mW, respectively. The amorphous area is approximately elliptical for the two cases, which is in agreement with the simulation results. It indicates that a high-power pulse can induce more volume into amorphous GST. However, as the pulse power is further increased, a larger amorphized zone is hard to be obtained. The temperature at the center of the GST-cell is much higher than its peripheral region, which results in severe degradation of the central part in the GST when its peripheral region reaches the melting point. The D1 (30-nm-thick GST) device, as explained in the previous part, has a higher attenuation of the optical transmission in both states. If one attempts to reach a higher transmission level in the amorphization process, multiple higher power optical pulses are needed to switch more volume of GST to the amorphous state. However, the GST cell will be irreversibly degraded, as shown in Fig. 6(b). We also experimentally compare the power consumption of the devices in the amorphization process. Figure 6(e) shows the transmission change as a function of pump pulse power for D1 (red line), and D2 (black line). The obtained switching contrast of both devices has a relatively linear response with increased pump pulse power. The amorphization threshold power is higher for a thinner GST cell. The power consumption of D2 is 2.5 times higher than that of D1. This is in good agreement with our simulation.

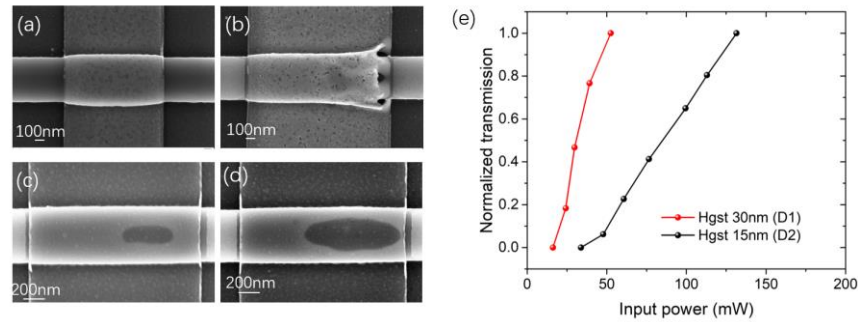


Fig. 6 (a, b) SEM images of the D1 (a) when the GST is in the original fully crystalline state, and (b) after multiple high-power optical pulses are applied. (c, d) SEM images of D2 when GST is amorphized by (c) a 75-mW optical pulse, and (d) a 150-mW optical pulse. (e) Transmission change as a function of optical pump optical pulse power.

2.3 Dynamic response to electrical pulses

Although the phase change under optical pulses exhibits a faster response speed, it is difficult to be employed in large-scale optical switch fabrics due to the inconvenient routing of the optical pump pulses. Instead, phase change under electrical pulses is more suitable since the electrical pulses can be delivered by electrical wires on another layer. To heat the GST cell using a microheater, we resort to the crossing structures, as shown in Fig. 7(a). The center of the crossing is covered by 30-nm-thick GST and 30-nm-thick ITO. The crossed silicon strip is heavily p^{++} -doped with a concentration of 10^{20} cm^{-3} so that it works as a resistive heater. A

Ti/Au (5nm/150nm) layer is deposited at two sides to provide an electrical connection. The gap size between the two Au electrodes is 5 μm . The crossed strips are 1 μm and 1.7 μm wide for the waveguide and MMI crossings, respectively. Figure 7(b) illustrates the optical wave propagation in the x - y plane for the waveguide and MMI crossings. The crossing induced loss for the regular waveguide and the MMI is 2.34 dB and 0.56 dB, respectively. The MMI crossing has a lower loss because the light is focused at the center due to the self-imaging principle of MMI.

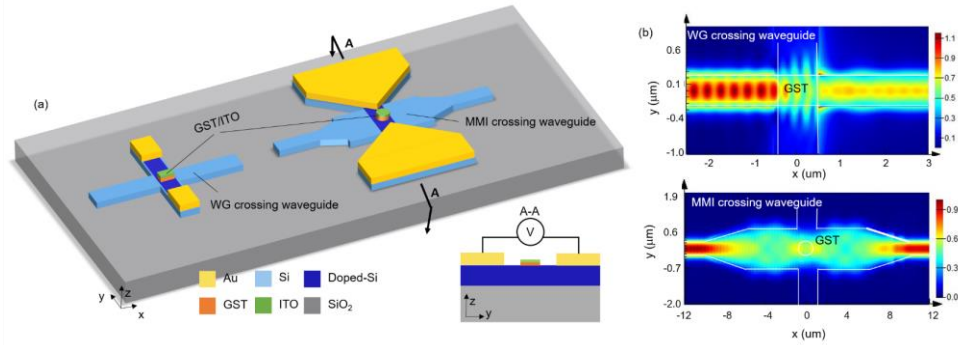


Fig. 7. (a) Strip waveguide crossing (left) and MMI crossing (right) integrated with electrically actuated GST. Inset: cross-section of the GST cell. (b) Simulated electrical field intensity distributions in the strip waveguide crossing (up) and the MMI crossing (bottom).

Next, we compare the maximum temperature distribution after electrical pulses are applied for the two crossings as a function of the peak voltage. Figure 8(a) shows the GST transient temperature response. The pulse duration is 20 ns and the peak voltage is 9 V and 11 V. The insets show the temperature profiles in the lateral cross-section of the GST layer. Due to the lower thermal dissipation, the strip waveguide crossing reaches a higher temperature compared with the MMI crossing. Figure 8(b) shows the temperature gradient along the ridgeline and the GST thickness direction as a function of the peak voltage. Under the same peak voltage, the temperature gradient along the ridgeline is larger than that along with the GST thickness. The temperature gradient for the strip waveguide crossing is larger than that for the MMI crossing. It should be noted that at a low peak voltage, the temperature gradient along the two directions is less than 100 $^{\circ}\text{C}$, suggesting that it is easier for an electrical pulse to induce phase change for the entire GST cell. This feature is quite different from the optical pulse excitation case, where the temperature gradient (especially along ridgeline) is still greater than 100 $^{\circ}\text{C}$ even at lower optical power. Figure 8(c) shows the transient temperature for two thicknesses of GST in response to an amorphization electrical pulse. The transient response is almost independent of the thickness of the GST film because the heating process is governed by the Joule heat transfer from the silicon resistive heater. In contrast, for optically induced phase change, the optical pump pulse evanescently interacts with the GST cell, and as a result, a thicker GST cell absorbs more light and reaches a higher temperature. Figure 8(d) shows the temperature gradient as a function of GST thickness. The temperature gradient along the ridgeline decreases with the GST thickness but that along the thickness direction increases with the GST thickness.

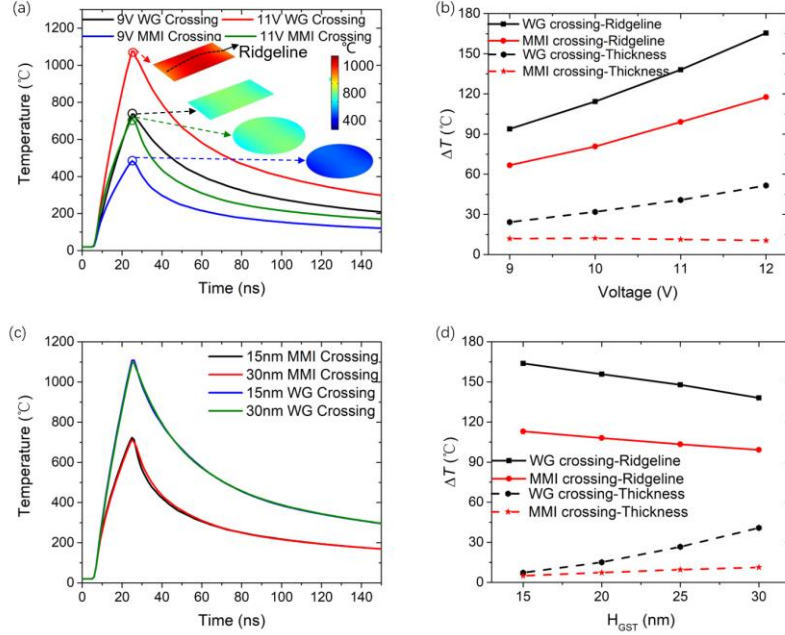


Fig. 8. (a) GST temperature variation in response to an excitation electrical pulse for the strip waveguide crossing and the MMI crossing. Insets: temperature profiles in the planar cross-section of the GST layer. (b) Temperature gradient along the ridgeline and the GST thickness direction as a function of the peak voltage. (c) GST temperature variation for two thicknesses of GST cell. (d) Temperature gradient along the ridgeline and the GST thickness direction as a function of GST thickness.

Table 2 summarizes the dynamic responses (energy efficiency, operation speed) and the basic optical properties (IL and ER) of the silicon waveguide and the MMI under optically and electrically induced phase change. The GST thickness is 30 nm. For many applications, a low IL and a large ER are required. We define the figure of merit as $FOM = (ER/IL)/V$, where V is the volume of the GST material. A high-performance device should have a high ER and a low IL and meanwhile, the GST cell should be as small as possible. For the optical phase transition, the strip waveguide can provide better performance with a higher FOM owing to the lower IL. For the electrical phase transition, the strip waveguide has a lower FOM mainly due to the loss from the crossed silicon strip. The crossing loss can be reduced if a PIN heater is used [29].

For the dynamic responses, the dead time of the optically induced phase change is shorter than that of the electrically induced phase change. For the optically induced phase change, GST temperature rises due to direct light absorption. Less energy is lost in the waveguide and substrate through thermal diffusion, and hence the dead time is shorter. We define energy efficiency as the ratio of the absorbed thermal energy in GST and the applied optical/electrical pulse energy, which is given by [46]

$$\eta = \frac{\int \rho C_p (T - 293) dV}{E_{pulse}} \quad (1)$$

where ρ is the GST density, C_p is the GST heat capacity, T is the temperature in kelvin unit, and E_{pulse} is the optical/electrical pulse energy. Figure 9 (a) and (b) show the energy efficiency for the optically and the electrically induced phase change, respectively. The energy efficiency increases with GST thickness. For the optically induced phase change, the energy efficiency of the MMI waveguide is lower than that of the strip waveguide because the large silicon area underneath the GST cell gives faster heat dissipation. For the electrically induced phase change, although the maximum temperature in the strip crossing is larger than that of MMI crossing, its

temperature gradient is also larger, and thus there is no significant difference in the GST absorbed heat energy, leading to almost the same energy efficiency. It should be noted that we only compare the operation speed and energy efficiency during the amorphization process since a single optical or electrical pulse can induce phase transition [42, 46, 47]. However, it is difficult to make a fair comparison of the operation speed and energy efficiency in the crystallization process. Optical excitation relies on evanescent field coupling to achieve phase transition. The state of GST influences the distribution of the optical field and thus the absorption of optical power, which ultimately affects the number of optical pulses and the total energy. Therefore, the crystallization process usually requires multiple optical pulses to get a complete phase transition. On the other hand, for the electrical excitation method, as the heater is formed by a doping silicon waveguide, the temperature gradient is much smaller than that in the optical excitation, and therefore a single pulse can be used in the crystallization process.

Table 2. Performance comparison of strip waveguide and MMI

Methods	Devices	IL (dB)	ER (dB)	FOM ($/\mu\text{m}^3$)	Energy efficiency * η	Dead time* (ns)
Optical excitation	Strip WG	0.21	11.58	3679.19	0.035	8
	MMI WG	0.59	12.85	924.36	0.021	6
Electrical excitation	Strip crossing	2.34	7.91	225.36	0.032	70
	MMI crossing	0.56	12.66	959.48	0.031	46

*under an amorphization pulse

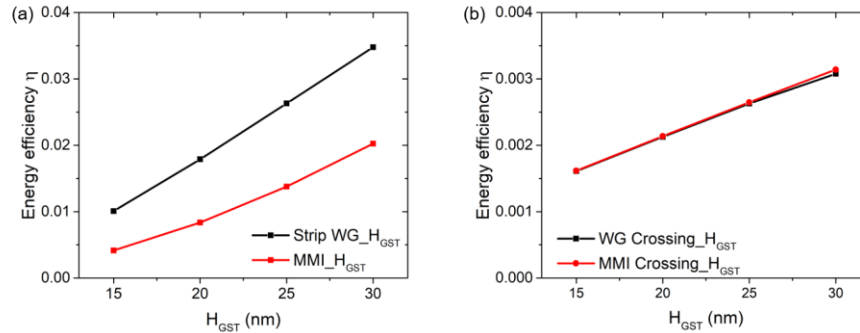


Fig. 9. Energy efficiency as a function of GST thickness in (a) optically induced phase change and (b) electrically induced phase change.

3. Conclusions

In conclusion, we have investigated the temperature distribution during the phase change process induced by optical and electrical pulses in the GST-loaded silicon strip waveguide and MMI. For optical pulse excitation, the strip waveguide has higher energy efficiency while the MMI presents a slightly faster operation speed. The difference is mainly caused by the high thermal dissipation of the MMI. However, optical pulse excitation is hard to be implemented in large-scale optical circuits, because it is very challenging to deliver optical pump pulses through waveguides to multiple GST sites in the circuit. This shortcoming can be resolved by using electrical pulse excitation where the electrical pump pulses can be applied locally through electrical connection wires. Our study reveals that the MMI crossing has a higher FOM and operation speed than the strip waveguide crossing under electrical pulse excitation.

4. Acknowledgments

This work was supported in part by the National key research and development program (2019YFB2203200, 2019YFB1802903, 2018YFB2201702), the National Natural Science

Foundation of China (NSFC) (6207030193), Shanghai Municipal Science and Technology Major Project (2017SHZDZX03), and the Open Project Program of Wuhan National Laboratory for Optoelectronics (2019WNLOKF004).

Disclosures

The authors declare that there are no conflicts of interest related to this article.

References

- [1] J. Wang, and Y. Long, "On-chip silicon photonic signaling and processing: a review," *Sci. Bull.* **2018**, *63*, 1267-1310.
- [2] S. Zhalehpour, M. Guo, J. Lin, Z. Zhang, H. Sepeshrian, Y. Qiao, W. Shi, and L. A. Rusch, "All silicon IQ modulator with 1Tb/s line rate," in *2020 Optical Fiber Communications Conference and Exhibition (OFC)*, 2020), 1-3.
- [3] X. Wang, L. Zhou, R. Li, J. Xie, L. Lu, K. Wu, and J. Chen, "Continuously tunable ultra-thin silicon waveguide optical delay line," *Optica* **2017**, *4*, 507-515.
- [4] W. Xu, L. Zhou, L. Lu, and J. Chen, "Aliasing-free optical phased array beam-steering with a plateau envelope," *Opt. Express* **2019**, *27*, 3354-3368.
- [5] P. Dumais, D. J. Goodwill, D. Celso, J. Jiang, C. Zhang, F. Zhao, X. Tu, C. Zhang, S. Yan, J. He, M. Li, W. Liu, Y. Wei, D. Geng, H. Mehrvar, and E. Bernier, "Silicon photonic switch subsystem with 900 monolithically integrated calibration photodiodes and 64-fiber package," *J. Lightwave Technol.* **2018**, *36*, 233-238.
- [6] K. Suzuki, R. Konoike, J. Hasegawa, S. Suda, H. Matsuura, K. Ikeda, S. Namiki, and H. Kawashima, "Low-insertion-loss and power-efficient 32×32 silicon photonics switch with extremely high- Δ silica PLC connector," *J. Lightwave Technol.* **2019**, *37*, 116-122.
- [7] Z. Guo, L. Lu, L. Zhou, L. Shen, and J. Chen, " 16×16 Silicon optical switch based on dual-ring-assisted Mach-Zehnder interferometers," *J. Lightwave Technol.* **2018**, *36*, 225-232.
- [8] L. Lu, S. Zhao, L. Zhou, D. Li, Z. Li, M. Wang, X. Li, and J. Chen, " 16×16 non-blocking silicon optical switch based on electro-optic Mach-Zehnder interferometers," *Opt. Express* **2016**, *24*, 9295-9307.
- [9] L. Qiao, W. Tang, and T. Chu, " 32×32 silicon electro-optic switch with built-in monitors and balanced-status units," *Sci. Rep.* **2017**, *7*, 42306.
- [10] V. Soriano, M. Midrio, G. Contestabile, I. Asselberghs, C. Van, J. Huyghebaert, I. Goykhman, A. K. Ott, A. C. Ferrari, and M. Romagnoli, "Graphene-silicon phase modulators with gigahertz bandwidth," *Nat. Photonics* **2018**, *12*, 40-44.
- [11] C. Haffner, W. Heni, Y. Fedoryshyn, J. Niegemann, A. Melikyan, D. L. Elder, B. Baeuerle, Y. Salamin, A. Josten, U. Koch, C. Hoessbacher, F. Ducry, L. Juchli, A. Emboras, D. Hillerkuss, M. Kohl, L. Dalton, C. Hafner, and J. Leuthold, "All-plasmonic Mach-Zehnder modulator enabling optical high-speed communication at the microscale," *Nat. Photonics* **2015**, *9*, 525-528.
- [12] J. Jeong, Y. Jung, Z. Qu, B. Cui, A. Khanda, A. Sharma, S. S. P. Parkin, and J. K. S. Poon, "VO₂ electro-optic memory and oscillator for neuromorphic computing," in *Conference on Lasers and Electro-Optics*, OSA Technical Digest (Optical Society of America, 2020), STh3R.2.
- [13] S. Abel, F. Eltes, J. E. Ortmann, A. Messner, P. Castera, T. Wagner, D. Urbonas, A. Rosa, A. M. Gutierrez, D. Tulli, P. Ma, B. Baeuerle, A. Josten, W. Heni, D. Caimi, L. Czornomaz, A. A. Demkov, J. Leuthold, P. Sanchis, and J. Fompeyrine, "Large pockels effect in micro- and nanostructured barium titanate integrated on silicon," *Nat. Materials* **2019**, *18*, 42-47.
- [14] H. Zhang, L. Zhou, B. M. A. Rahman, X. Wu, L. Lu, Y. Xu, J. Xu, J. Song, Z. Hu, L. Xu, and J. Chen, "Ultracompact Si-GST hybrid waveguides for nonvolatile light wave manipulation," *IEEE Photonics J.* **2018**, *10*, 1-10.
- [15] V. J. Sorger, N. D. Lanzillotti-Kimura, R. Ma, and X. Zhang, "Ultra-compact silicon nanophotonic modulator with broadband response," *Nanophotonics* **2012**, *1*.
- [16] Y. Zhang, J. Chou, J. Li, H. Li, Q. Du, A. Yadav, S. Zhou, M. Y. Shalaginov, Z. Fang, H. Zhong, C. Roberts, P. Robinson, B. Bohlin, C. Ríos, H. Lin, M. Kang, T. Gu, J. Warner, V. Liberman, K. Richardson, and J. Hu, "Broadband transparent optical phase change materials for high-performance nonvolatile photonics," *Nat. Commun.* **2019**, *10*, 4279.
- [17] J. Feldmann, N. Youngblood, C. D. Wright, H. Bhaskaran, and W. H. P. Pernice, "All-optical spiking neurosynaptic networks with self-learning capabilities," *Nature* **2019**, *569*, 208-214.
- [18] C. Wu, H. Yu, S. Lee, R. Peng, I. Takeuchi, and M. Li, "Programmable phase-change metasurfaces on waveguides for multimode photonic convolutional neural network," *arXiv:2004.10651* **2020**.
- [19] J. Feldmann, N. Youngblood, M. Karpov, H. Gehring, X. Li, M. L. Gallo, X. Fu, A. Lukashchuk, A. Raja, J. Liu, C. D. Wright, A. Sebastian, T. Kippenberg, W. H. P. Pernice, and H. Bhaskaran, "Parallel convolution processing using an integrated photonic tensor core," *arXiv:2002.00281* **2020**.
- [20] I. Chakraborty, G. Saha, A. Sengupta, and K. Roy, "Toward fast neural computing using all-Photonic phase change spiking neurons," *Sci. Rep.* **2018**, *8*, 12980.
- [21] P. Xu, J. Zheng, J. K. Doylend, and A. Majumdar, "Low-loss and broadband nonvolatile phase-change directional coupler switches," *ACS Photonics* **2019**.

- [22] C. Wu, H. Yu, H. Li, X. Zhang, I. Takeuchi, and M. Li, "Low-loss integrated photonic switch using subwavelength patterned phase change material," *ACS Photonics* **2019**, *6*, 87-92.
- [23] Q. Zhang, Y. Zhang, J. Li, R. Soref, T. Gu, and J. Hu, "Broadband nonvolatile photonic switching based on optical phase change materials: beyond the classical figure-of-merit," *Opt. Lett.* **2018**, *43*, 94-97.
- [24] Y. Ikuma, Y. Shoji, M. Kuwahara, X. Wang, K. Kintaka, H. Kawashima, D. Tanaka, and H. Tsuda, "Small-sized optical gate switch using Ge₂Sb₂Te₅ phase-change material integrated with silicon waveguide," *Electron. Lett.* **2010**, *46*, 368-U5480.
- [25] X. Li, N. Youngblood, C. Ríos, Z. Cheng, C. D. Wright, W. H. P. Pernice, and H. Bhaskaran, "Fast and reliable storage using a 5 bit, nonvolatile photonic memory cell," *Optica* **2019**, *6*, 1-6.
- [26] C. Ríos, M. Stegmaier, P. Hosseini, D. Wang, T. Scherer, C. D. Wright, H. Bhaskaran, and W. H. P. Pernice, "Integrated all-photon non-volatile multi-level memory," *Nat. Photonics* **2015**, *9*, 725.
- [27] H. Zhang, L. Zhou, J. Xu, N. Wang, H. Hu, L. Lu, B. M. A. Rahman, and J. Chenn, "Nonvolatile waveguide transmission tuning with electrically-driven ultra-small GST phase-change material," *Sci. Bull.* **2019**.
- [28] C. R. Galarreta, A. M. Alexeev, Y. Au, M. Lopez-Garcia, M. Klemm, M. Cryan, J. Bertolotti, and C. D. Wright, "Nonvolatile reconfigurable phase-change metadevices for beam steering in the near infrared," *Adv. Funct. Mater.* **2018**, *28*, 1704993.
- [29] J. Zheng, Z. Fang, C. Wu, S. Zhu, P. Xu, J. K. Doylend, S. Deshmukh, E. Pop, S. Dunham, M. Li, and A. Majumdar, "Nonvolatile electrically reconfigurable integrated photonic switch enabled by a silicon PIN diode heater," *Adv. Mater.* **2020**, *32*, 2001218.
- [30] M. H. Lankhorst, B. W. Ketelaars, and R. A. Wolters, "Low-cost and nanoscale non-volatile memory concept for future silicon chips," *Nature Mater.* **2005**, *4*, 347-352.
- [31] H. S. P. Wong, S. Raoux, S. Kim, J. Liang, J. P. Reifenberg, B. Rajendran, M. Asheghi, and K. E. Goodson, "Phase change memory," *Proc. IEEE* **2010**, *98*, 2201-2227.
- [32] M. Wuttig, and N. Yamada, "Phase-change materials for rewriteable data storage," *Nature Mater.* **2007**, *6*, 824-832.
- [33] K. Makino, J. Tominaga, and M. Hase, "Ultrafast optical manipulation of atomic arrangements in chalcogenide alloy memory materials," *Opt. Express* **2011**, *19*, 1260-1270.
- [34] A. V. Kolobov, P. Fons, A. I. Frenkel, A. L. Ankudinov, J. Tominaga, and T. Uruga, "Understanding the phase-change mechanism of rewritable optical media," *Nature Mater.* **2004**, *3*, 703-708.
- [35] X. Li, N. Youngblood, Z. Cheng, S. G.-C. Carrillo, E. Gemo, W. H. P. Pernice, C. D. Wright, and H. Bhaskaran, "Experimental investigation of silicon and silicon nitride platforms for phase-change photonic in-memory computing," *Optica* **2020**, *7*, 218-225.
- [36] M. Stegmaier, C. Ríos, H. Bhaskaran, C. D. Wright, and W. H. P. Pernice, "Nonvolatile all-optical 1 × 2 switch for chipscale photonic networks," *Adv. Opt. Mater.* **2017**, *5*, 1600346.
- [37] M. Rudé, J. Pello, R. E. Simpson, J. Osmond, G. Roelkens, J. J. G. M. van der Tol, and V. Pruneri, "Optical switching at 1.55 μm in silicon racetrack resonators using phase change materials," *Appl. Phys. Lett.* **2013**, *103*, 141119.
- [38] M. Stegmaier, C. Ríos, H. Bhaskaran, and W. H. P. Pernice, "Thermo-optical effect in phase-change nanophotonics," *ACS Photonics* **2016**, *3*, 828-835.
- [39] J. Feldmann, M. Stegmaier, N. Gruhler, C. Ríos, H. Bhaskaran, C. D. Wright, and W. H. P. Pernice, "Calculating with light using a chip-scale all-optical abacus," *Nat. Commun.* **2017**, *8*, 1256.
- [40] K. Kato, M. Kuwahara, H. Kawashima, T. Tsuruoka, and H. Tsuda, "Current-driven phase-change optical gate switch using indium-tin-oxide heater," *Appl. Phys. Express* **2017**, *10*, 072201.
- [41] D. Tanaka, Y. Shoji, M. Kuwahara, X. Wang, K. Kintaka, H. Kawashima, T. Toyosaki, Y. Ikuma, and H. Tsuda, "Ultra-small, self-holding, optical gate switch using Ge₂Sb₂Te₅ with a multi-mode Si waveguide," *Opt. Express* **2012**, *20*, 10283-10294.
- [42] C. Ríos, M. Stegmaier, Z. Cheng, N. Youngblood, C. D. Wright, W. H. P. Pernice, and H. Bhaskaran, "Controlled switching of phase-change materials by evanescent-field coupling in integrated photonics [Invited]," *Opt. Mater. Express* **2018**, *8*, 2455-2470.
- [43] A. Redaelli, A. Pirovano, A. Benvenuti, and A. L. Lacaita, "Threshold switching and phase transition numerical models for phase change memory simulations," *J. Appl. Phys.* **2008**, *103*, 111101.
- [44] F. Xiong, A. D. Liao, D. Estrada, and E. Pop, "Low-power switching of phase-change materials with carbon nanotube electrodes," *Science* **2011**, *332*, 568-570.
- [45] H. Zhang, L. Zhou, L. Lu, J. Chen, and B. M. A. Rahman, "Optical computing and logic operation with GST-enabled silicon photonics," in *2019 Asia Communications and Photonics Conference (ACP)*, 2019), 1-3.
- [46] J. Zheng, S. Zhu, P. Xu, S. Dunham, and A. Majumdar, "Modeling electrical switching of nonvolatile phase-change integrated nanophotonic structures with graphene heaters," *ACS Appl. Mater. & Inter.* **2020**, *12*, 21827-21836.
- [47] J. Zheng, A. Khanolkar, P. Xu, S. Colburn, S. Deshmukh, J. Myers, J. Frantz, E. Pop, J. Hendrickson, J. K. Doylend, N. Boechler, and A. Majumdar, "GST-on-silicon hybrid nanophotonic integrated circuits: a non-volatile quasi-continuously reprogrammable platform," *Opt. Mater. Express* **2018**, *8*, 1551.